ACES Asian Chemical Editorial Society

doi.org/10.1002/cnma.202300356

CHEMNANOMAT
Research Article

www.chemnanomat.org

Probing the Behavior of Composition-Tunable Ultrathin PtNi Nanowires for CO Oxidation and Small-Molecule Electrocatalytic Reactions

Nathaniel Hurley,[a] Michael Gallagher,[a] Christopher Koenigsmann,[b] Elena Stephanie,[a] Monireh Davoudi,[a] Anna M. Plonka,[c] Haodong Wang,[c] Lihua Zhang,[d] Anatoly I. Frenkel,*[c, e] and Stanislaus S. Wong*[a]

We have successfully synthesized ultrathin nanowires of pure Pt, $Pt_{99}Ni_1$, Pt_9Ni_1, and Pt_7Ni_3 using a modified room-temperature soft-template method. Analysis of both methanol oxidation reaction (MOR) and ethanol oxidation reaction (EOR) results found that the Pt_7Ni_3 samples yielded the best performance with specific activities of 0.36 and 0.34 mA/cm^2 respectively. Additionally, formic acid oxidation reaction (FAOR) tests noted that both Pt and PtNi nanowires oxidize small organic molecules (SOMs) via an indirect pathway. CO oxidation data suggests little measurable performance without any pre-reduction treatment; however, after annealing in H_2, we detected significantly improved CO_2 formation for both Pt_9Ni_1 and Pt_7Ni_3 motifs. These observations highlight the importance of pre-treating these nanowires under a reducing atmosphere to enhance their performance for CO oxidation. To explain these findings, we collected extended x-ray adsorption fine structure (EXAFS) spectroscopy data, consistent with the presence of partial alloying with a tendency for Pt and Ni to segregate, thereby implying the formation of a Pt-rich shell coupled with a Ni-rich core. We also observed that the degree of alloying within the nanowires increased after annealing in a reducing atmosphere, a finding deduced through analysis of the coordination numbers and calculations of Cowley's short range order parameters.

Introduction

In this study, we investigated structure-property correlations with respect to the catalytic properties of Pt-based ultrathin nanowire (NW) alloys. Platinum is typically used as a high-performance fuel cell catalyst to convert chemical energy into electrical energy. However, the widespread use of Pt is problematic for several reasons, including its very high cost, comparatively low abundance, poor long-term stability, surface oxidation, vulnerability to metal dissolution, and susceptibility to CO poisoning under standard operating conditions. Hence, approaches towards creating a novel, highly stable, and well-performing catalyst have relied on replacing platinum-group metals (PGMs) with more plentiful, less expensive, and potentially less hazardous non-PGM alternatives, such as but not limited to Ni.

In this context and in this paper, we have chosen to investigate various compositions of ultrathin PtNi NW alloys, incorporating more highly abundant Ni species. Ultrathin NWs are anisotropic 1D motifs with average diameters of 10 nm or less. The crystal structure of Pt NWs has been previously reported as face-centered cubic (*fcc*) with a space group of Fm-3 m.[1] Ultrathin NWs are expected to maintain slightly contracted surfaces, which can weaken the interaction with O_2 and prevent passivation of the electrocatalyst by O_2.[2–4] The extended, smooth facets associated with an anisotropic morphology coupled with high surface area-to-volume ratios are also beneficial for catalytic applications. In addition, to highlight their promise as a nanoscale platform, ultrathin NWs may also be more chemically homogeneous, uniform, and structurally monodisperse, while maintaining fewer defect sites as compared with commercial bulk and nanoparticle (NP) analogues. Moreover, alloying of Pt with cheaper elements further reduces the amount of Pt needed and thereby lowers the overall cost. Indeed, via alloy formation, the precise nature of the second element can not only modify the *d band* structure and electron density of Pt through a "ligand effect" but also

[a] Dr. N. Hurley, M. Gallagher, E. Stephanie, M. Davoudi, Prof. S. S. Wong
Department of Chemistry
Stony Brook University
Stony Brook, New York 11794-3400 (USA)
E-mail: stanislaus.wong@stonybrook.edu
Homepage: http://www.stonybrook.edu/commcms/wonggroup/

[b] Prof. C. Koenigsmann
Department of Chemistry
Fordham University
Bronx, NY 10458 (USA)

[c] Dr. A. M. Plonka, H. Wang, Prof. A. I. Frenkel
Department of Materials Science and Chemical Engineering
Stony Brook University
Stony Brook, New York 11794-2275 (USA)
E-mail: anatoly.frenkel@stonybrook.edu
Homepage: https://you.stonybrook.edu/frenkel/

[d] Dr. L. Zhang
Center for Functional Nanomaterials, Building 735
Brookhaven National Laboratory
Upton, New York 11973 (USA)

[e] Prof. A. I. Frenkel
Chemistry Division, Building 555
Brookhaven National Laboratory
Upton, New York 11973 (USA)

Supporting information for this article is available on the WWW under https://doi.org/10.1002/cnma.202300356

create a compression strain induced by the incorporation of Ni atoms into the underlying Pt lattice.[5,6] Finally, alloying can improve stability and reduce poisoning by reducing the binding energy of CO onto the NW's external surface.[7]

As relevant precedence in the field, we have successfully synthesized stable, ultrathin formulations of monometallic, bimetallic, and core@shell NWs, consisting of Pt, Pd, $Pd_{1-x}Ni_x$, $Pd_{1-x}Cu_x$, $Pd_{1-x}Au_x$, $Pd_{1-x}Pt_x$, Pd@Pt, and Pd_9Au@Pt in past work.[4,8–17] Moreover, we have produced not only Ru@Pt core@shell NWs[18] but also ultrathin, ternary PtRuFe NWs.[19] To synthesize the wires in our current study, we have used a room temperature, solution-based method to create worm-like networks of ultrathin NWs of both Pt and PtNi. Production of the latter motif was modified from our previous work on ternary PtRuFe NWs by replacing Ru and Fe precursors with the appropriate Ni-containing reagent.[19] This method is advantageous, since it can be performed under ambient temperature and pressure conditions, is easily scalable, and results in reliable composition control by carefully and systematically varying the molar ratios of the initial Pt and Ni precursors. Other procedures, that have been used to create PtNi alloys, include hydrothermal,[20,21] solid-state,[22,23] and room-temperature protocols.[24] However, many of these syntheses, specifically those based on hydrothermal and solid-state reactions, use either high temperatures and/or high pressures to generate the PtNi alloys. By contrast, our technique is relatively fast as compared with the other previously reported processes, since the addition of $NaBH_4$ as the reducing agent can cause the wires to form essentially instantaneously.

As implied earlier, both monometallic Pt and the Pt-based alloys have demonstrated a high intrinsic activity with respect to many types of reactions. Our group has had significant experience with using ultrathin NW alloys for small molecule oxidation and other types of catalytic reactions.[17,18,25,26] As such, our objective in this work has been to extend this body of knowledge by systematically probing the composition-dependent performance of a family of Pt_xNi_{1-x} NW-based alloys using a variety of relevant liquid-phase electrocatalytic reactions, including the methanol oxidation reaction (MOR), the ethanol oxidation reaction (EOR), and the formic acid oxidation reaction (FAOR).

In addition to all these electrocatalytic measurements, we have also analyzed this material for its gas-phase CO oxidation ability. This reaction was chosen, because the byproducts of small molecule oxidation include CO, which can poison Pt sites and significantly reduce activity. This process renders the removal of CO as key to the creation of high performing catalysts; consequently, understanding gas phase CO removal will provide us with insight into the ability of our PtNi alloys to remove CO by its conversion to CO_2.[27,28] Due to the relative simplicity of this reaction, the performance can be measured simply by accounting for and monitoring the partial pressure changes of either CO or O_2. However, most of the research done on Pt-based alloys for CO oxidation has been performed on NPs,[27,28] indicating a gap in the literature that we have addressed by analyzing our different compositions of unique ultrathin PtNi NW motifs.

As a means of addressing these crucial issues, we have collected X-ray absorption spectroscopy (XAS) data on our systems. Specifically, we have considered a combination of X-ray absorption near edge structure (XANES) and extended X-ray absorption fine structure (EXAFS) spectroscopy to acquire both electronic and structural information, respectively, about the material. XANES provides information about the oxidation state of the X-ray absorbing atoms, while EXAFS focuses on the coordination environment of the absorbing atoms, thereby revealing relevant information about the coordination numbers, distances, and type of atoms surrounding the absorbing atoms.[2,29–32] Previously, we have studied Pt-based ultrathin NW alloys, including but not limited to RuPt and PtPd using XAS.[33] This prior work with Ru_1Pt_1 demonstrated that, whereas energy dispersive spectroscopy (EDS) analysis implied homogeneous alloy formation, the complementary EXAFS data were consistent with a tendency towards 'clustering' of like elements. Conversely, both EDS and EXAFS supported the formation of homogeneous mixtures of Pt and Pd within the Pd_1Pt_9 sample. Indeed, we showed the importance of a holistic consideration of both EXAFS and High-resolution transmission electron microscopy energy dispersive spectroscopy (HRTEM EDS) as a means for properly understanding the structure of alloy NWs.[33] We continue to pursue this goal herein by applying EXAFS and EDS to the study of PtNi alloys of varying compositions to understand their structure and to use all of this information to rationalize our suite of catalytic results.

The novelty of this work therefore centers on the methodical testing of the catalytic activity of different compositions of ultrathin PtNi NWs. We have systematically varied the chemical composition of our ultrathin NWs from pure Pt, $Pt_{99}Ni_1$, Pt_9Ni_1 to Pt_7Ni_3 and demonstrated their intrinsic viability for the MOR, EOR, and FAOR processes. Moreover, we are the first to report gas phase CO oxidation data with respect to the PtNi ultrathin NW system. Finally, we have collected EXAFS and HRTEM EDS data for the samples, prior to and after reduction with 5% H_2, and reported on the observed physical and chemical changes. These cumulative results will lead to an improved understanding of the catalytic performance not only of PtNi ultrathin NWs as a specific case but also of ultrathin alloyed bimetallic systems as a more general example.

Results and Discussion

Synthesis and characterization

Ultrathin NWs have been synthesized using a solution-based, soft template technique. In this methodology, the ultrathin wires grow at the interface between water and chloroform within soft micellar templates formed *in-situ* by the presence of an ionic surfactant, namely hexadecyltrimethylammonium bromide (CTAB). Sodium borohydride ($NaBH_4$) is used as a reducing agent to reduce Pt^{4+} and Ni^{2+} to Pt^0 and Ni^0, respectively. Different precursor molar ratios of Pt and Ni were reacted to generate a series of NWs associated with pure Pt, $Pt_{99}Ni_1$, Pt_9Ni_1, and Pt_7Ni_3, respectively. Figure 1 provides an

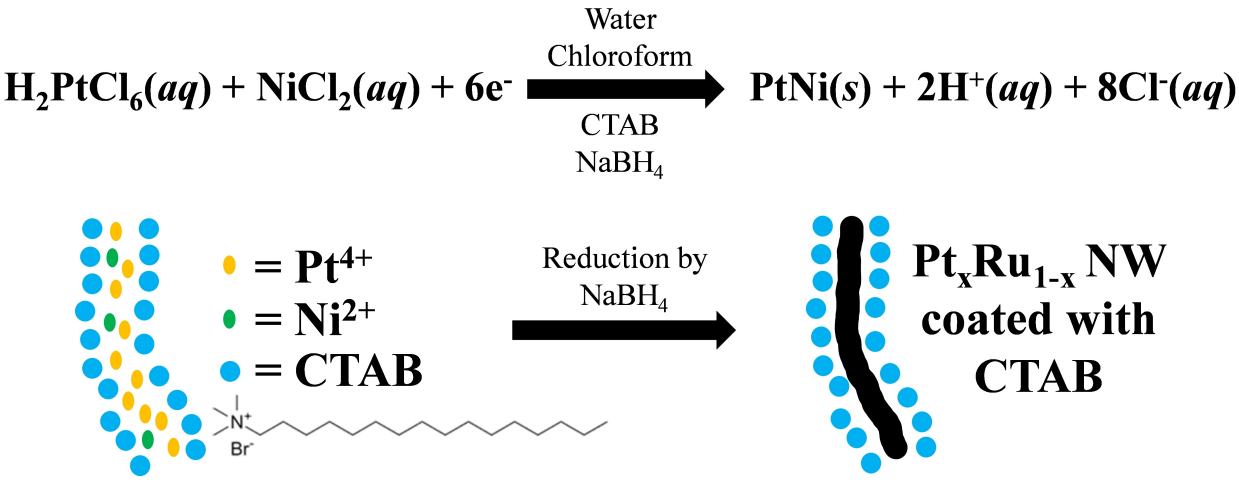

Figure 1. Chemical equation and illustration, highlighting the PtNi nanowire growth mechanism.

overview of the growth mechanism and the associated chemical equation, providing information about the formation of these ultrathin nanowires. Figure 2 highlights the TEM images and Figure S1 presents the corresponding size distributions of the various ultrathin, as-prepared NWs. These Pt and PtNi wires possessed a relatively consistent average diameter of 2.5 ± 0.5 nm.

To confirm the successful alloying of the wires, we obtained X-ray diffraction (XRD) data. All of these samples evinced the expected XRD pattern of fcc Pt (Figure 3). Specifically, no peaks from either nickel or nickel-containing compounds appeared, implying that the Ni was incorporated within the wires and did not segregate into discrete impurity phases. Further confirmation of the alloying process came from the high angular annular darkfield EDS (HAADF EDS) mapping data, provided in Figure 4. In particular, the elemental mapping profile for Pt indicates the presence of pure Pt with some oxygen on the surface (Figure 4A–D). We note that all samples likely have some oxygen on the surface. This is demonstrated by the partially oxidized nature of the Ni, as implied by XAS results, which are discussed in a subsequent section. Figure 4E–H, 3I–L, and 3M–P depicts EDS mapping data for Pt_9Ni_1, $Pt_{99}Ni_1$, and Pt_7Ni_3 respectively. Herein, the Pt and Ni signals closely overlap and superimpose on each other, suggestive of the expected and relatively homogeneous distribution of the elements throughout the entirety of the wires. However, with both the Pt_9Ni_1 and Pt_7Ni_3 samples, we observed a degree of Ni segregation as compared with the corresponding distribution of Pt. Overall, these findings support the conclusion that alloys of PtNi likely successfully formed in our synthesis, albeit with some segregation of elements for certain specific compositions.

XAS

To confirm the results provided by HAADF EDS mapping and to understand the local structure and compositional distribution of these alloyed nanowires more thoroughly, we studied our various ultrathin NWs using XAS. Data for the pre-and post-reduction samples, acquired at the Pt L_3 edge for the Pt_9Ni_1 and $Pt_{99}Ni_1$ NWs as compared with the Pt foil, are presented in Figure S2. Figures S2A and B provide the XANES region. Data in both r-space and k-space are given in Figures S2C–D and S2E–F, respectively. The XANES plots of the Pt L_3 edge (Figure S2A–B) indicate that the Pt is in the metallic phase. The relative peak heights in both k and r space are lower for the ultrathin NWs, denoting greater disorder and/or lower coordination numbers as compared with the bulk counterpart, both factors being indicative of the nanoscale morphology of the wires. Additionally, when comparing the r-space plots of the NWs both before and after the reduction process, we note that the post-reduction sample intensity is in between the magnitudes of the pre-reduction and the foil signals. This intermediate intensity is an indication that after it had been annealed at 300 °C for 2 hours, sintering within the sample had occurred. A consequence of that observation is that the Pt–Ni coordination number (CN) was found to increase. This finding may be plausibly ascribed to a passivation of the surface, due to an increased aggregation induced by the annealing process, thereby leading to an increased coordination noted around individual atoms. To demonstrate this thermal sintering and aggregation effect, we obtained TEM images of Pt_9Ni_1 both before and after H_2 treatment (Figure S3).

Figure S4A, C, and E highlight the XANES and EXAFS data for the Ni K edges for both Pt_9Ni_1 in energy, k, and r space respectively. $Pt_{99}Ni_1$ data for energy, k, and r space are given in Figures S4B, D, and F, respectively. Herein we include the data for the NiO and the metallic Ni control samples as references. We observed the expected nanoscale effects on the EXAFS data in the wires as compared with their bulk counterparts, with lower intensities noted in the nanowire EXAFS data as compared with that of the corresponding bulk. However, the white line of the Ni K edges appears to be situated in-between those of Ni and NiO. This finding suggests that the Ni is partially oxidized, even after the reduction step.

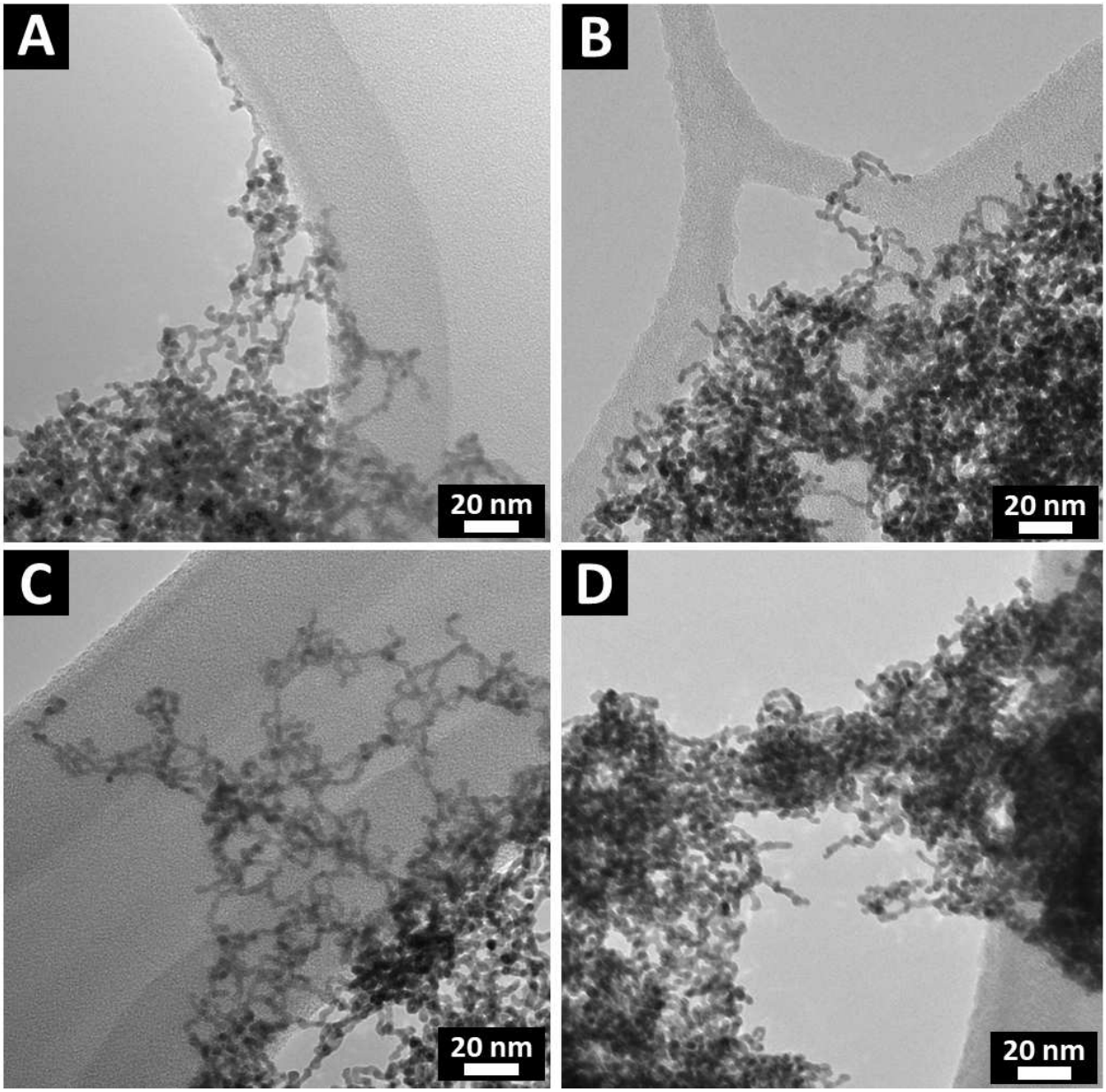

Figure 2. TEM images of as-prepared alloyed NWs, including (A) pure Pt, (B) $Pt_{99}Ni_1$, (C) Pt_9Ni_1, and (D) Pt_7Ni_1.

The Artemis program was used to fit the experimental data.[34] For pure Pt wires, the fitting results for the Pt L_3 edge are given in Table S1. The fits in r- and k-spaces are shown in Figure S5. Here we observe a coordination number of 8.6. The coordination number for bulk Pt is 12; as such, the reduced coordination number of Pt within our anisotropic motifs is consistent with the smaller number of nearest neighbors, which we would expect for an ultrathin nanowire with a size range of 2–3 nm. The fits of the $Pt_{99}Ni_1$ Pt L_3 edge are provided in Table S2, and the associated plots are shown in Figure S6. The coordination number computed for the sample prior to reduction (i.e., pre-reduction) is 9, whereas after the reduction process (i.e. post-reduction), it was calculated to be 10.3. This finding implies an enlargement in the average volume around the Pt atoms, thereby resulting in the lowering of the surface-to-volume ratio, after the reduction step. This volume expansion may be due either to an aggregation of the wires or to a thermally-induced sintering effect.

The only Ni K edge spectra that could be fit were the post-reduction Ni K EXAFS data for the $Pt_{99}Ni_1$ sample. These fitting results are found in Table S3 and Figure S7. Due to the low loading of Ni and the concomitant poor signal quality, the analysis of Ni edge was performed separately from that of the Pt edge. In addition, it should be noted that no reasonable fit could be obtained for the pre-reduction Ni K edge for $Pt_{99}Ni_1$, due to noise.

For the Pt_9Ni_1 sample, we performed a multiple dataset fitting algorithm, using both the Ni K and Pt L_3 edges. This process has been reported earlier and successfully used many times in the successful analysis of multi-elemental

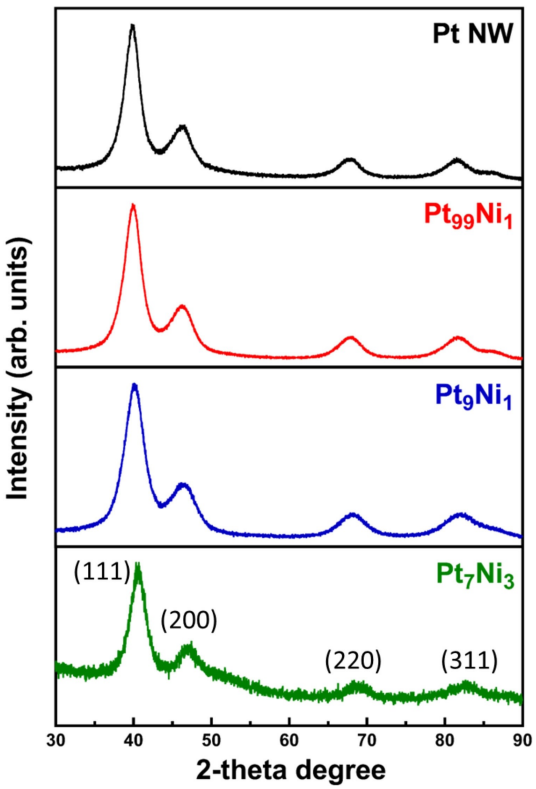

Figure 3. XRD patterns, pertaining to the composition of various as-synthesized NWs.

systems.[2,31,35–37] The fitting results for the Ni K and Pt L_3 edges are tabulated in Tables 1 and 2, respectively. These tables also include Ni and Pt foil fitting data, which were used to obtain the best fit values for the amplitude factor (S_0^2). Figures 5 and 6 contain the final fits for the Ni K and Pt L_3 samples.

From all of these combined results, we can derive several conclusions about the materials. Specifically, coordination numbers can be used to determine the structure of the material as well as the degree of alloying. Our XRD and HRTEM EDS data collectively suggest that Ni is dispersed within the platinum lattice analogous to that of an alloy. However, these methods

Table 1. XAS data for Pt_9Ni_1 NWs. Values are presented for Ni *K*-edge multi-data set fitting. Results are generated for samples, prepared both before and after reduction in 5% H_2.

Parameter	Fitting result Ni Foil	Pt_9Ni_1 (Ni K edge) Post-reduction	Pt_9Ni_1 (Ni K edge) Pre-reduction
N_{NiNi}	12	4.5 ± 1.6	6.6 ± 1.6
N_{NiPt}	N/A	7.0 ± 1.6	5.4 ± 1.6
S_0^2	0.80 ± 0.04	0.80	0.80
ΔE_0 [eV]	−0.9 ± 0.5	−4.7 ± 1.1	−3.8 ± 1.1
R_{NiNi} [Å]	2.484 ± 0.003	2.619 ± 0.025	2.629 ± 0.026
R_{NiPt} [Å]	N/A	2.635 ± 0.014	2.640 ± 0.013
σ^2_{NiNi} [Å^2]	0.0060 ± 0.0003	0.0353 ± 0.0097	0.0238 ± 0.0039
σ^2_{NiPt} [Å^2]	N/A	0.0116 ± 0.0024	0.0088 ± 0.0029

Table 2. XAS data for Pt_9Ni_1 NWs. Values are presented for Pt L_3 edge multi-data set fitting. Results are generated for samples, prepared both before and after reduction in 5% H_2.

Parameter	Fitting result Pt Foil	Pt_9Ni_1 (Pt L_3 edge) Post-reduction	Pt_9Ni_1 (Pt L_3 edge) Pre-reduction
N_{PtPt}	12	9.5 ± 0.6	7.9 ± 0.7
N_{PtNi}	N/A	0.8 ± 0.4	0.7 ± 0.3
S_0^2	0.85 ± 0.03	0.85	0.85
ΔE_0 [eV]	8.8 ± 0.4	7.0 ± 0.4	6.2 ± 0.5
R_{PtPt} [Å]	2.766 ± 0.002	2.741 ± 0.002	2.741 ± 0.002
R_{PtNi} [Å]	N/A	2.637 ± 0.014	2.647 ± 0.014
σ^2_{PtPt} [Å^2]	0.0048 ± 0.0002	0.0066 ± 0.0003	0.0066 ± 0.0003
σ^2_{PtNi} [Å^2]	N/A	0.0083 ± 0.0029	0.0088 ± 0.0029

do not have sufficient levels of sensitivity to precisely detect the local compositional details of how uniform the dispersion of Ni actually is throughout the nanostructure. These important nuances in the spatial composition can vary dramatically to encompass diverse, plausible scenarios, such as but not limited to the clustering of 'like' atoms in addition to the random distribution of alloy components.[2,32,38–40]

To determine the degree of homogeneity in the nanowires, we need to compute and differentiate the total coordination numbers of A–M and B–M (A, B – the alloying components, M = A or B) from the partial coordination numbers of N_{AA}, N_{AB}, N_{BB}, and N_{BA} [Eqs. (1)&(2)].[34]

$$N_A = N_{AA} + N_{AB} \quad (1)$$

$$N_B = N_{BB} + N_{BA} \quad (2)$$

In our case, A = Pt and B = Ni.[41] If N_A and N_B are equal, then the elements are functionally equivalent and there is no real preference for spatial segregation, implying the presence of homogeneity. Conversely, if N_A is either greater than or less than N_B, then there is poor mixing between the two atom types; as such, it is evident that the larger the difference between these coordination numbers, the greater the corresponding heterogeneity in the resulting alloy which would be expected and the more likely that elemental segregation will occur.

Based on equations 1 and 2 therefore, we calculated the total coordination numbers of Pt and Ni for Pt_9Ni_1 which are provided in Table 3. Under "pre-reduction" reaction conditions, we observe N_{Pt} = 8.6 and N_{Ni} = 12. This finding implies that there is segregation present between the Pt and Ni atoms, with Ni preferentially situated at the fully coordinated, sub-surface sites. For the "post reduction"- processed samples, N_{Pt} = 10.3 and N_{Ni} = 11.5. The decrease in the numerical difference between the total coordination numbers of the Pt and Ni atoms is suggestive of a corresponding increase in the homogeneity of the resulting alloy. It is worth noting that the formation of a homogeneous alloy is consistent with previous reports for PtNi nanoparticles that had been thermally treated in an H_2 atmosphere.[42]

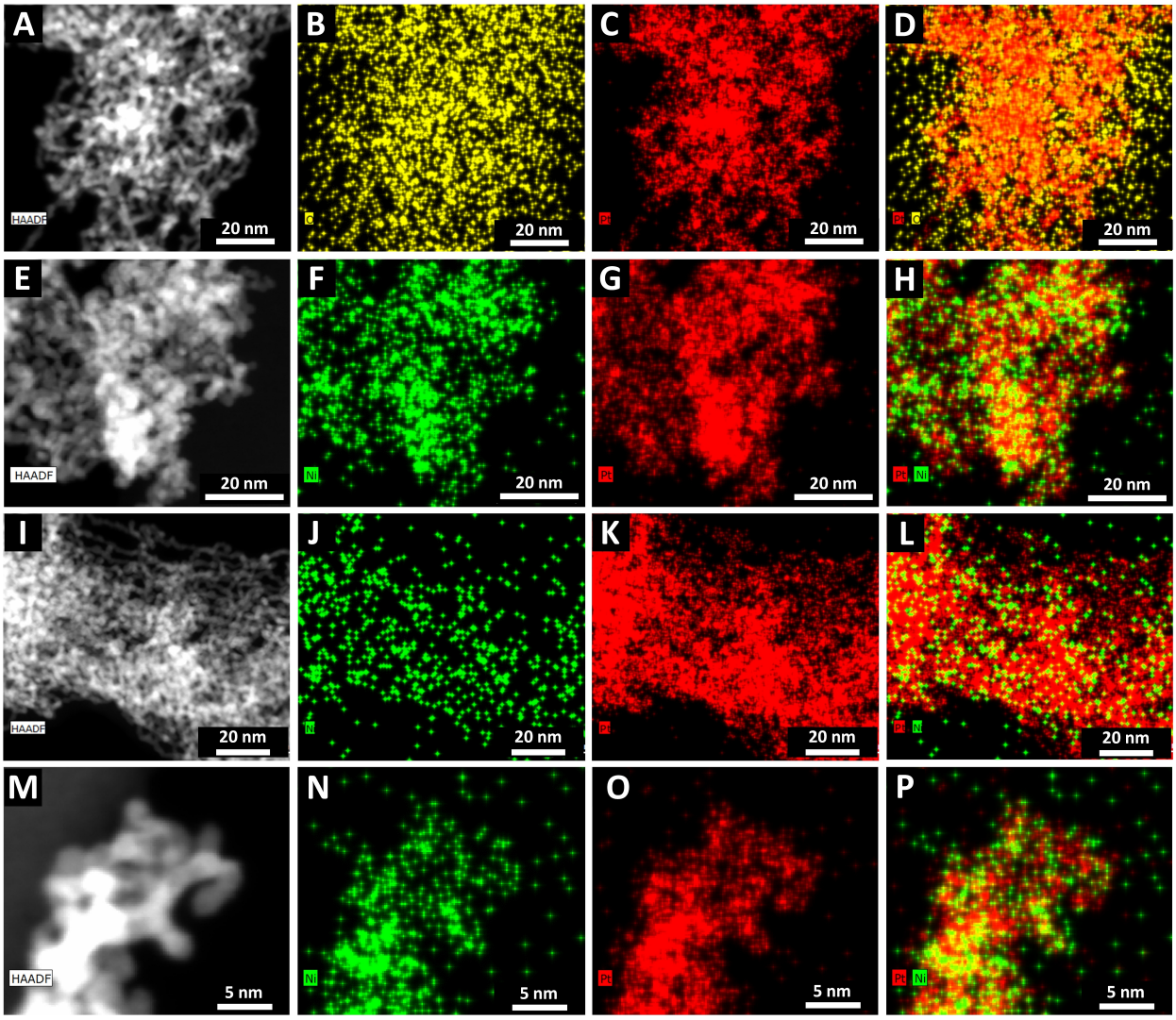

Figure 4. HAADF images and HRTEM EDS mapping data, associated with the different chemical compositions of NWs including. (A–D) refer to the pure Pt HAADF image, O signal mapping, Pt mapping signal, and a combined overlay of Pt–O, respectively. (E–H) pertain to the HAADF, Ni mapping, Pt mapping, and Pt–Ni overlay results for Pt_9Ni_1, respectively. (I–L) highlight the HAADF, Ni mapping, Pt mapping, and Pt–Ni overlay data for $Pt_{99}Ni_1$, respectively. Finally, (M–P) are associated with the HAADF, Ni mapping, Pt mapping, and Pt–Ni overlay results for Pt_7Ni_3, respectively.

Table 3. Total coordination numbers, chemical composition data derived from EXAFS, and the short-range order parameters.

Sample	N_{Pt}	N_{Ni}	X_{Pt}	X_{Ni}	α_{PtNi}	α_{NiPt}
Pt_9Ni_1 Pre-reduction	8.6 ± 0.8	12 ± 2.3	0.89 ± 0.06	0.11 ± 0.06	0.26 ± 0.18	0.49 ± 0.17
Pt_9Ni_1 Post-reduction	10.3 ± 0.7	11.5 ± 2.1	0.90 ± 0.05	0.10 ± 0.05	0.22 ± 0.16	0.32 ± 0.10

Additionally, we can make use of and interpret the trends in the total coordination numbers to determine if the elements are preferentially located either in the core or the shell of the as-prepared material or are in a mixed state. In general, if N_A is larger than N_B then we can presume that the A species is mainly localized in the core and that the shell is rich with the B species and vice versa. For the 'pre-reduction' sample, we find that N_{Ni} is larger than N_{Pt}. Since the EXAFS analysis does not indicate a complete segregation of the elements, we can assert that the as-prepared nanowires most likely possess a Ni-rich core coupled with a Pt-rich shell, but they do not necessarily form "perfect" core-shell structures. An alternative explanation is that Ni is preferentially located in the sub-surface sites, while Pt is more uniformly distributed throughout the nanowire. Both models are consistent with the distribution of the coordination numbers obtained by EXAFS analysis. Both models agree that there is a relatively stronger degree of segregation of Pt and Ni at the surface for the pre-reduction sample as compared with

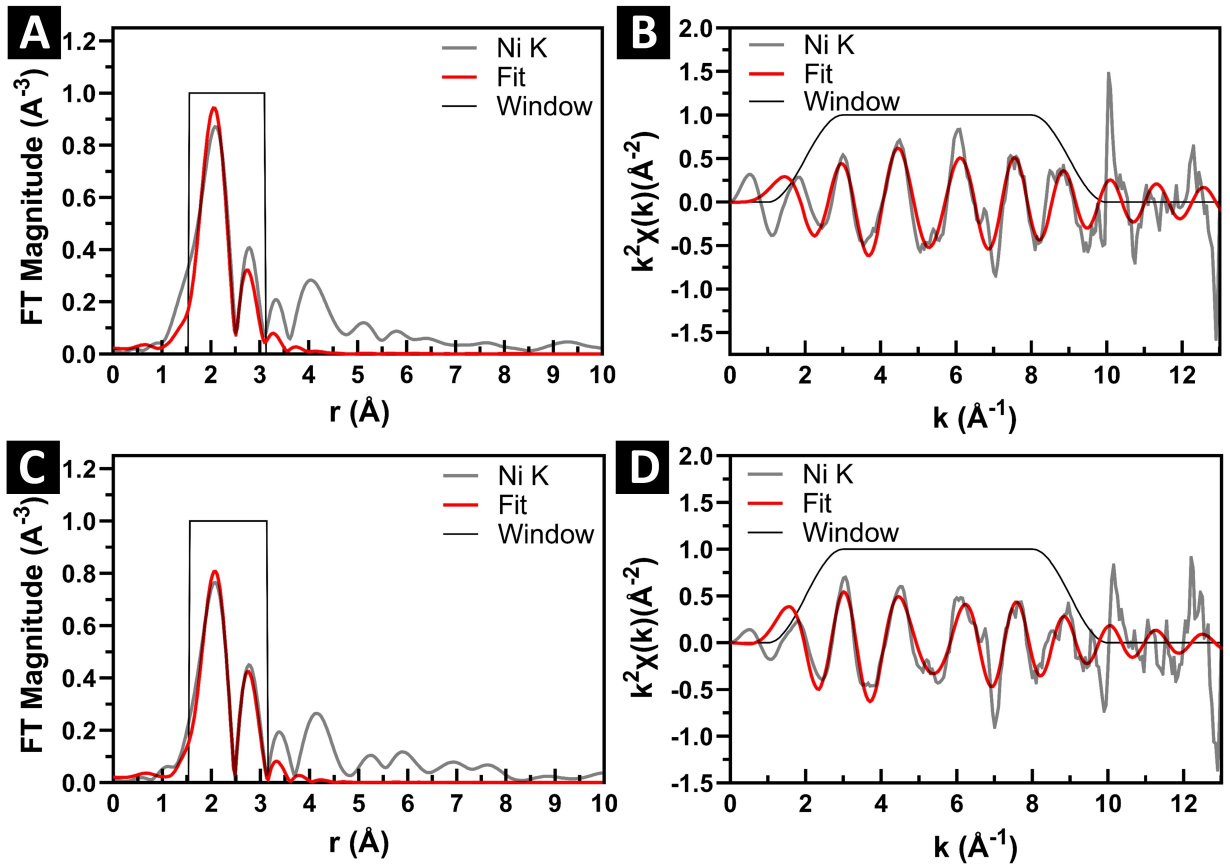

Figure 5. XAS spectra for Pt_9Ni_1 NWs. Data are presented for Ni *K*-edge multi-data set fitting. (A) R-space pre-reduction, (B) K-space pre-reduction, (C) R-space post-reduction, and (D) K-space post-reduction.

the post-reduction one, because the difference between the total coordination numbers in the "post-reduction" sample is smaller as compared with its "pre-reduction" counterpart.

Hence, we used the Cowley short range order parameter (SRO) to better quantify and understand the degree of alloying within our as-prepared nanowires.[32] When the alloys are relatively homogeneous, the degree of the short range order for each component (A or B) can be evaluated. That is, at short-range, we can figure out the concentrations of species A and B (x_A and x_B), as follows:

$$\frac{x_B}{x_A} = \frac{N_{AB}}{N_{BA}}, \qquad x_A + x_B = 1 \tag{3}$$

Using Equations (1), (2), and (3), we computed the corresponding Cowley's short range order parameter, α, as follows:[2,32,43,44]

$$\alpha_{AB} = 1 - \frac{N_{AB}/N_A}{x_B} \tag{4}$$

The results derived from Equations (1), (2), (3), and (4) are provided in Table 3. Based on the examination of the short-range order parameter, we can state that if the **α** value is $-1 < \alpha_{AB} < 0$, then there is a negative tendency for clustering. If $\alpha_{AB} = 0$, then a perfectly random alloy was formed. Finally, if $0 < \alpha_{AB} < 1$, then there is a tendency for the A atoms to segregate and cluster.[32] The SRO values for the Pt_9Ni_1 samples that had been subject to "pre-reduction" were found to be 0.26 and 0.49 for α_{PtNi} and α_{NiPt}, respectively. These positive values appear to indicate a tendency for both Pt and Ni atoms to preferentially cluster, thereby leading to the generation of a less homogeneous alloy. This finding aligns with the prior analysis focused on the coordination numbers alone. For samples subjected to "post reduction" treatment, we observed a shift to lower values of α_{PtNi} and α_{NiPt}, namely 0.22 and 0.32 respectively. This outcome suggests the expected presence of an increased degree of alloying, after heating at 300 °C within a 5% H_2 atmosphere. The change in the α_{PtNi} however is very small and within the calculated error, so it cannot be conclusively determined if this change is meaningful.

Electrochemistry

To understand and correlate the effect of systematically tuning the amount of Ni content on the resulting electrochemical performance, we varied the amount of Ni relative to that of Pt within as-prepared ultrathin NWs. We compared these results to those obtained from pure Pt NWs alone, made with the same

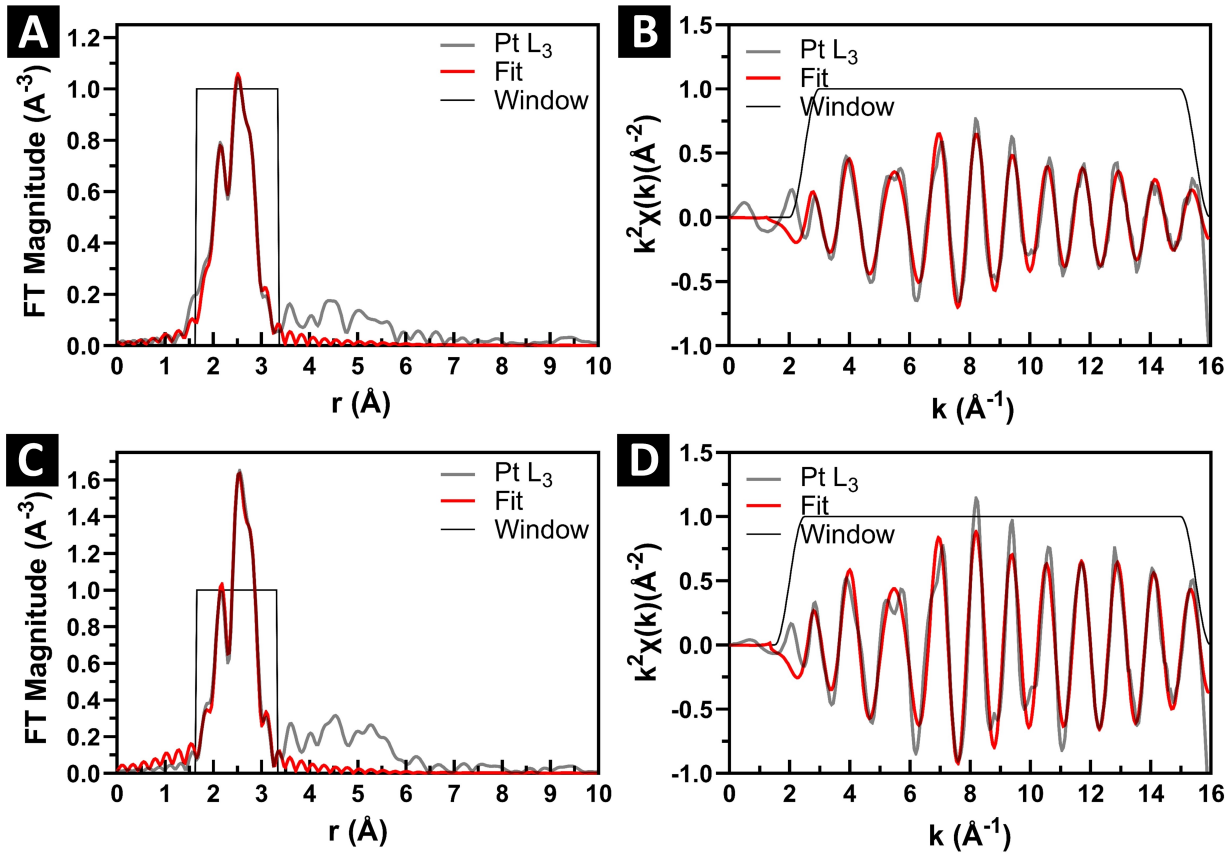

Figure 6. XAS spectra for Pt_9Ni_1 NWs. Data are presented for Pt L_3 edge multi-data set fitting. (A) R-space pre-reduction, (B) K-space per-reduction, (C) R-space post-reduction, and (D) K-space post-reduction.

synthetic method. We deposited these wires onto Vulcan carbon XC-72 with a loading of about 20%. To confirm the predicted loading values, we used thermogravimetic analysis (TGA) to remove the Vulcan carbon and to assess the remaining Pt content (Figure S8). Values obtained from the TGA were used to calculate the electrocatalytic surface area and other measurements impacted by the loading. Inks of these samples were then deposited onto the glassy carbon electrodes for subsequent MOR, EOR, and FAOR testing.

Cyclic voltammetry (CV) curves for the Pt and PtNi ultrathin nanowires are provided in Figure 7. All of the curves show the expected hydrogen adsorption and desorption (0–0.2 V) peaks as well as the formation and reduction of the oxide layer (06/6–1.0 V), associated with Pt. The position of the oxide reduction peak on the cathodic sweep was measured by fitting a Gaussian function to the peak. We found that the oxide reduction peak position fluctuated from 0.783 V, 0.784 V, 0.779 V, and 0.786 for Pt NWs, $Pt_{99}Ni_1$, Pt_9Ni_1, and Pt_7Ni_3, respectively. The variation in the oxide peak is relatively small and suggests that the Ni content does not result in a significant change in the adsorption strength of oxygen.

Additionally, we computed the specific surface area (SSA) values, which were determined by integrating the hydrogen adsorption and desorption regions in the CVs. For NWs of Pt, $Pt_{99}Ni_1$, Pt_9Ni_1, and Pt_7Ni_3, the corresponding SSA values were noted to be 12.52, 12.78, 9.08, and 6.45 m^2/g, respectively. Nickel and its oxides are not stable in acidic media and thus, the decline in SSA cannot solely be attributed to Ni atoms replacing Pt atoms at the interface. However, the structural reconfiguration that occurs once the nanowires are immersed in the acidic electrolyte and Ni is etched from the surface may result in a degree of aggregation of the nanowires. To better understand the effect of the catalysis on the morphological evolution of the wires, we obtained TEM images, both before and after the electrochemical tests were run. These data are presented in Figure S9 for the nanowire sample and in Figure S10 for the Pt/C commercial standard. All of these samples show the presence of NWs that had been deposited onto Vulcan carbon, prior to electrochemical testing. We noted that, after the electrochemical runs, the isolated samples appeared to be significantly more aggregated, thereby suggesting some degree of morphological degradation over time, during the measurement process. As a possible explanation, Ni is known to leach from the Pt NWs upon application of an external potential, a scenario conducive to reconfiguring the NW morphology, consistent with our data.

Methanol, Ethanol, and Formic acid Oxidation

The MOR linear sweep voltammetry (LSV) measurements, chronoamperometry, and bar graphs with error bars are

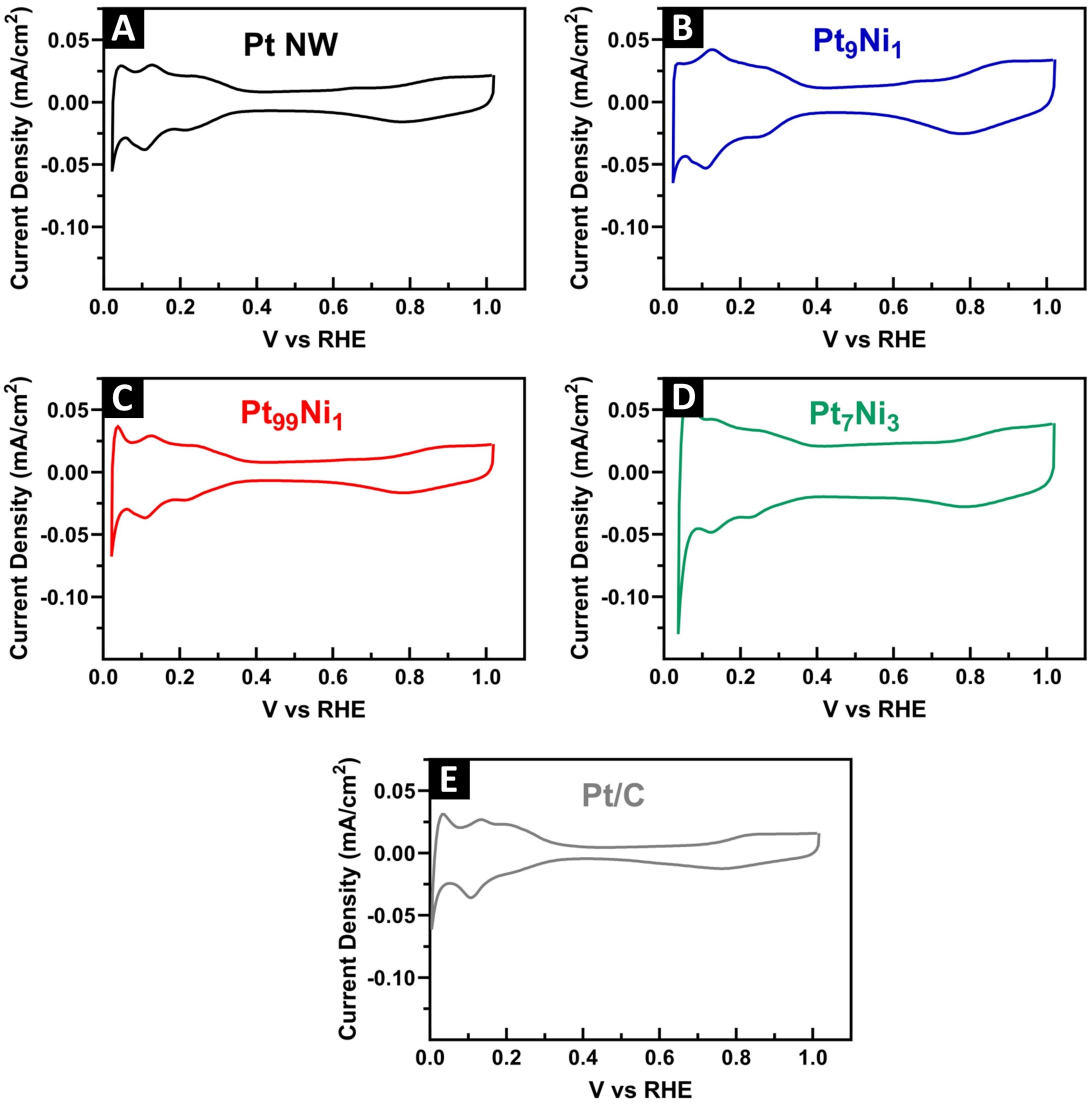

Figure 7. CV data collected for NWs of (A) pure Pt, (B) Pt_9Ni_1, (C) $Pt_{99}Ni_1$, and (D) Pt_7Ni_3, in addition to (E) commercial Pt/C, respectively.

provided in Figure 8A, B, and C respectively. Table 4 summarizes the MOR activities for the as-prepared samples. The specific activity values for the Pt/C commercial standard, Pt NWs alone, $Pt_{99}Ni_1$, Pt_9Ni_1, and Pt_7Ni_3 were found to be 0.17, 0.30, 0.26, 0.26, and 0.36 mA/cm^2, measured respectively at 0.7 V vs. RHE. This set of observations indicates that at low levels (i.e. ~10% or less), the nickel content appears to do little if anything to enhance the MOR performance as compared with that of pure Pt NWs alone. Interestingly though, increasing the nickel content to 30% resulted in a small measurable increase in the measured specific activity relative to the corresponding specific activity, observed for the sample with only 10% nickel. To further our understanding of the observed changes with respect to MOR, we collected complementary chronoamperometry measurements which probe sample stability.

Figure 9 provides a comparison of the mass activities of the as-synthesized samples analyzed by MOR and EOR. By contrast with the improvement in specific activity (SA) of our nanowires with respect to the commercial Pt/C standard, the mass activities we have measured herein are significantly lower than those of the commercial Pt/C for both MOR and EOR. We propose that this finding arises from a combination of two possible factors: the presence of aggregation and surfactants. We note in the TEM images in Figures S9 and S10, that the wires are somewhat aggregated prior to the electrochemical tests, and that the degree of aggregation increases after the tests are run. This observation means that although our samples maintain a relatively high SA, comparable to the prior literature, the mass activity (MA) is low, because a large number of active sites are physically trapped within the aggregates. That is, these potentially active sites are unavailable and inaccessible, and as such, are unable to contribute to the observed performance.[18] With respect to the surfactants, prior reports have indicated that chemical pre-treatments are needed to completely remove them.[26] However, if there were residual CTAB molecules on the external surfaces of the wires due to an incomplete washing step, then this would also act to block active sites, thereby resulting in lower MA values relative to those associated with

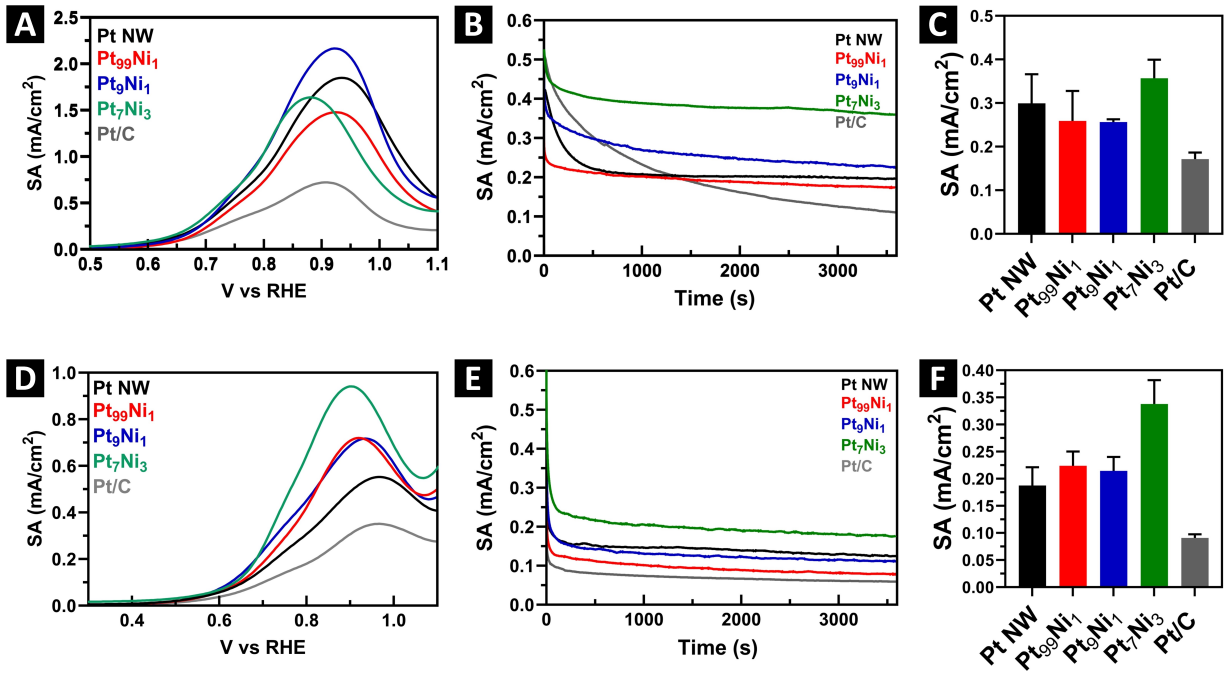

Figure 8. MOR: (A) chronoamperometry data taken at 0.7 V, (B) linear sweep voltammetry (LSV) measurements, and (C) associated bar graphs showing the computed SA values. **EOR**: (D) chronoamperometry data taken at 0.7 V, (E) linear sweep voltammetry (LSV) measurements, and (F) associated bar graphs highlighting the calculated SA values. All of the SA values discussed herein were obtained at 0.7 V vs RHE.

Table 4. MOR and EOR results associated with NWs of Pt, $Pt_{99}Ni_1$, Pt_9Ni_1, and Pt_7Ni_3, including specific activity, and specific surface area. Additionally, the peak positions from a Gaussian fit of the oxide reduction peak from the CV are also included for each sample.

Material (ultrathin NW motif)	Specific activity [mA/cm^2] for MOR	Specific activity [mA/cm^2] for EOR	Specific Surface Area [m^2/g]	Oxide reduction peak position
Pt/C commercial standard	0.17@0.7 V 0.58@0.85 V	0.09@0.7 V 0.22@0.85 V	74.21	0.762 V
Pt	0.30@0.7 V 1.41@0.85 V (vs. RHE)	0.19@0.7 V 0.43@0.85 V (vs. RHE)	12.52	0.783 V
$Pt_{99}Ni_1$	0.26@0.7 V 1.28@0.85 V (vs. RHE)	0.22@0.7 V 0.59@0.85 V (vs. RHE)	12.78	0.784 V
Pt_9Ni_1	0.26@0.7 V 1.30@0.85 V (vs. RHE)	0.21@0.7 V 0.68@0.85 V (vs. RHE)	9.08	0.779 V
Pt_7Ni_3	0.36@0.7 V 1.49@0.85 V (vs. RHE)	0.34@0.7 V 1.50@0.85 V (vs. RHE)	6.45	0.786 V

commercial Pt. That is, we would expect to observe a lower MA, even if the SA is still high, because SA is intrinsically a function and measure of the available active sites. Therefore, the combination of both aggregation and the presence of surfactant in inhibiting reagent access to active sites would almost certainly have resulted in a low MA value, as indeed was noted in our data.

Chronoamperometry can give insight into the electrochemical durability of our materials. Specifically, the chronoamperometry data were acquired at 0.7 V vs. RHE for a duration for 3600 s, with the associated results provided in Figure 8B. All of the samples evince an initial drop, which can be potentially attributed to the rapid dehydrogenation of methanol and the corresponding buildup of CO on the surface. All nanowire samples also reach a higher steady state specific activity than the Pt/C commercial standard. Based on these cumulative results, we observed a direct correlation between the amount of Ni and the associated steady state SA value. Specifically, we found that the Pt_7Ni_3 species gave rise to the highest steady state reading, followed by that of Pt_9Ni_1. This finding confirms that the addition of Ni decreases the steady state coverage of CO in the onset region and leads to faster MOR kinetics. Both $Pt_{99}Ni_1$ and pure Pt yielded the lowest and almost identical

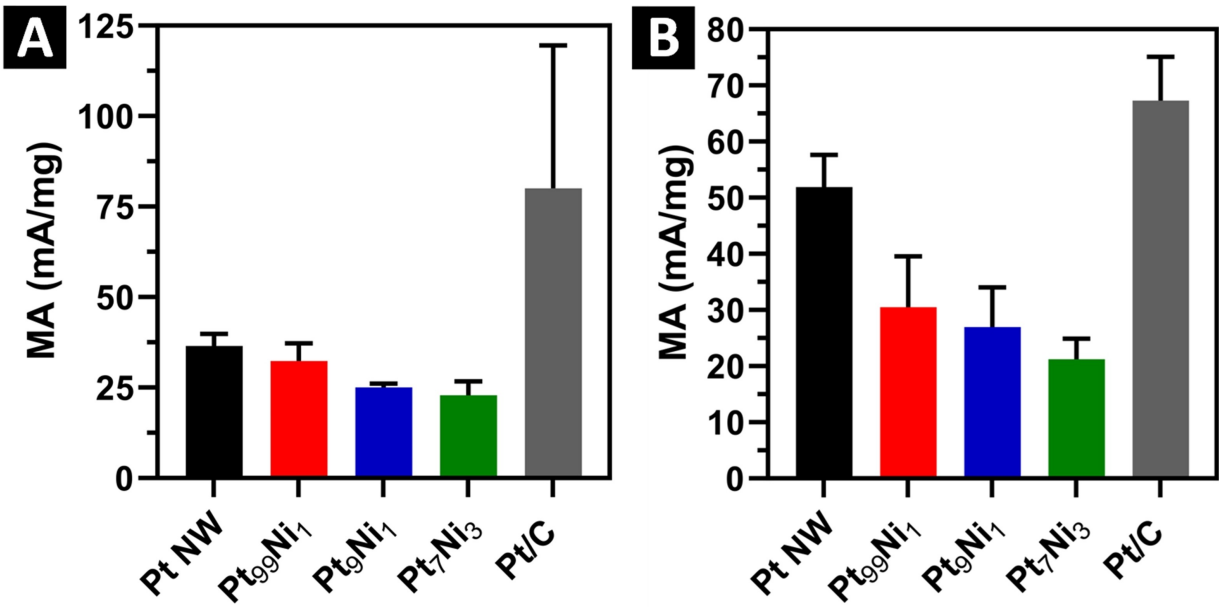

Figure 9. Mass activities of all ultrathin nanowire samples as compared with commercial Pt/C for (A) MOR and (B) EOR.

steady state SA quantities, which are in line with the relatively higher proportions of Pt within these latter samples.

Based on the prior literature, there are several possible explanations for the increased activity resulting from the presence of nickel content, such as either a bifunctional effect arising from outer, exposed Ni sites if the Ni is indeed present at the surface or an electronic effect if the nickel is passivated within the nanowire core.[45] Considering the first possibility, increases in MOR activity have been attributed to a bifunctional effect, derived from the presence of more oxophilic metals present at the surface in alloys such as ruthenium. However, in this case, Ni and its oxides are not stable in acidic media, and are therefore unlikely to be present at the outer surface after the first few electrochemical cycles.[46] Moreover, the XAS results indicate that Ni is already localized in the core of the nanowire after synthesis.

Thus, a more likely explanation for the increased performance can be ascribed to the electronic effects that are derived from the presence of Ni inside the alloy and the structural effects of localizing Ni within the core of the nanostructure. The XAS data in Figure S2 corroborate this explanation, since the L_3 absorption peaks (white line) are more intense in the Pt_9Ni and $Pt_{99}Ni$ nanowires than the analogous peak for Pt foil. This finding is indicative of a higher degree of Pt *d*-band vacancy arising from the electronic interactions between the Ni and the Pt, and this observation is correlated with a weaker binding of adsorbates such as CO through both experimental and computational results.[47,48] Weakening the interaction with CO should reduce the impact of CO poisoning during small molecule oxidation, since CO oxidation can proceed with a lower degree of oxygen coverage and therefore, at a lower overpotential. Based on the trend in MOR activity, the data suggests that a minimum of 30% Ni within the nanostructure is necessary for the electronic effect to sufficiently weaken the binding of CO and to thereby lead to a measurable change in the onset of methanol oxidation. Table S4 provides for a comparison between our MOR results and those of other analogous PtNi compositions, reported in the prior literature.

The corresponding LSV measurements, chronoamperometry, and associated bar graphs with error bars for our EOR results are given in Figure 8D, E, and F, respectively. EOR LSV data and the accompanying results for the EOR measurements indicate that the specific activity values for NWs of Pt, $Pt_{99}Ni_1$, Pt_9Ni_1, and Pt_7Ni_3 were noted to be 0.19, 0.22, 0.21, and 0.34 mA/cm^2, respectively, at 0.7 V vs. RHE. As with the MOR, there is little change observed between the SA values of Pt, $Pt_{99}Ni_1$, and Pt_9Ni_1, thereby suggesting that relatively low Ni contents (i.e., ~10% or less) are insufficient to generate a greater catalytic activity beyond that of standard Pt wires. In line with this argument, we observed a much greater EOR activity for the Pt_7Ni_3 sample. SI Figure 9B provides bar graphs for the mass activity measurements. Table S5 compares our EOR results with those of other similar PtNi compositions in the past literature.

Platinum-based catalysts typically follow the indirect pathway wherein SOMs are rapidly dehydrogenated, thereby forming CO as the primary intermediate. Although formic acid is not the primary intermediate in the indirect pathway, FAOR is useful in determining the mechanism of SOM oxidation and the apparent effectiveness of a catalyst. Formic acid is the primary intermediate in the direct oxidation pathway of methanol. In this pathway, formic acid is rapidly formed and is then directly converted to CO_2 via a subsequent slower oxidation step. Although formic acid is not the primary intermediate in the complementary indirect pathway, FAOR is still useful in determining the mechanism of SOM oxidation and the apparent effectiveness of a catalyst. Hence, to better understand the CO tolerance and mechanism of the MOR, we

collected LSVs in a solution of formic acid and the results are provided in Figure 10.

Catalysts that oxidize SOMs via a direct pathway will have a peak localized at 0.6 V, and this peak denotes the direct oxidation of formic acid to CO_2. Conversely, catalysts that oxidize SOMs via the indirect pathway will preferentially convert formic acid to CO, thereby leading to a distinctive oxidation wave at 0.9 V consistent with the oxidation of CO to CO_2 after the onset of Pt surface oxidation. Since Pt-based catalysts have a high density of Pt–Pt pair sites, they tend to oxidize SOMs via the indirect pathway, thereby giving rise to a characteristic indirect oxidation peak at 0.9 V with a shoulder that extends to 0.4 V.[49]

In this case, the pure platinum catalyst's LSV is consistent with that observed in the literature for platinum catalysts and confirms that SOM oxidation likely proceeds via an indirect pathway. The addition of Ni to the catalysts leads to changes to both the peak at 0.9 V and the shoulder that extends to 0.4 V. Focusing on the peak at 0.9 V, increasing Ni content results in a 100 mV shift in the peak to lower potentials. A shift in this peak indicates that the activation of CO formed by the indirect oxidation of formic acid is more facile on the nanowires containing nickel. Shifting the focus to the shoulder of the oxidation wave, the Pt_9Ni and Pt_7Ni_3 catalysts maintain a higher activity over the entire region that is associated with the direct oxidation of formic acid to CO_2 (0.4 V–0.8 V). The increase in activity in this region could be a consequence of a higher degree of the direct oxidation of formic acid, resulting from the nickel content present. However, our CO stripping results suggests that increasing the nickel content can lower the overall coverage of CO. Thus, it is more likely that the higher activity in this region arises from more Pt active sites being available for formic acid oxidation, since CO coverage is reduced. This result is also consistent with the higher MOR and EOR kinetics in the onset region of the MOR LSV.

To explain the values of our MOR, FAOR, and EOR results that we observed with our Pt, $Pt_{99}Ni_1$, and Pt_9Ni_1 samples, we analyzed these data in the context of our EXAFS findings. It was determined through an analysis of the coordination numbers of the Pt_9Ni_1 sample, that Ni is situated preferentially in the core while Pt tends to be localized in the shell. If this is the case, then the surfaces of the wires are largely unchanged from that

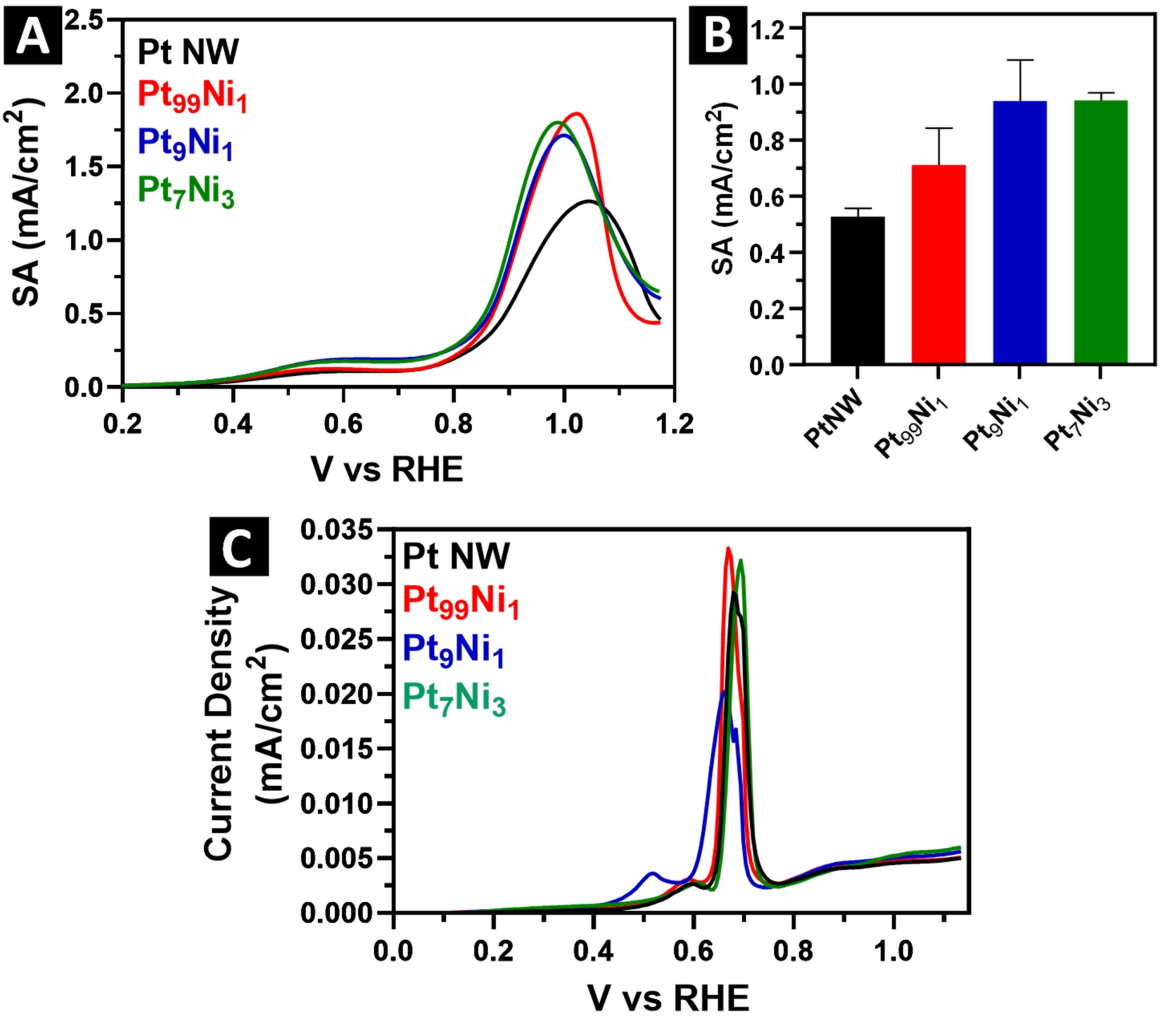

Figure 10. (A) LSV measurements and (B) the corresponding SA values for the FAOR process at 0.9 V. (C) CO stripping data are presented for all nanowire samples.

of pure Pt alone, and as such, the Ni will have little contact with the organic molecular entities present during the catalysis process. Accordingly, we would have expected that all wires would behave in a similar manner to that of pure Pt, in the sense that Ni is not contributing to a bifunctional effect.

For the Pt_7Ni_3 sample, we can hypothesize that the amount of Ni was sufficiently high enough that even though Ni was preferentially found in the core, there was in fact ample Ni content within the shell to yield a clear catalytic enhancement with respect to the other samples. Our XAS results reveal that the Ni content contributes to a measurable electronic effect that increases Pt *d*-band vacancies, the latter of which tend to be associated with weaker CO binding and better CO tolerance. In addition, the EXAFS results reveal that increasing Ni content contributes to higher degrees of disorder in the nanowire structure. More lattice disorder could also lead to a greater density of defect sites at the surface, which oxidize at lower potentials and can facilitate CO oxidation.

We performed CO stripping measurements to evaluate the CO tolerance of the catalysts. The stripping voltammograms (Figure 10C) depict a primary oxidation wave and an associated shoulder at lower potentials. The shoulder likely arises from oxidation of CO adsorbed either to defect sites or to higher energy facets potentially localized at the ends of the wires. The position of the main peak of the PtNi samples is generally consistent with the peak position for Pt, suggesting that the addition of Ni does not facilitate activation of CO at lower overpotentials. However, the incorporation of Ni does lower the coverage of CO, as Ni content increases. We compared the CO stripping charge to the H_{ads} charge from cyclic voltammetry to determine the relative coverage of CO. We found that the relative coverage of CO (in relation to the H_{ads} charge) was 78.0%, 73.9%, and 65.7% for the $Pt_{99}Ni_1$, Pt_9Ni_1, and Pt_7Ni_3 catalysts, respectively, signifying decreasing CO coverage with increasing Ni content. With respect to pure Pt NWs, the measured coverage was 67.7%, which was higher in magnitude as compared with the 65.7% reading for the Pt_7Ni_3 catalyst. CO poisoning arises from the high degree of CO coverage, present at low overpotentials.[50,51] Therefore, the fact that the presence of Ni lowers the coverage of CO can thereby lead to the higher steady state MOR activity, observed in the chronoamperometry results detected for the PtNi catalysts.

Gas phase CO oxidation

CO oxidation measurements were obtained before and after the H_2 reduction process. Based on the results provided in Figure 11, we observed little if any alteration in the amount of CO_2 produced at all of the temperatures tested. After annealing at 300 °C for 2 h in 5% H_2, there was little to no change observed in the amount of CO_2 produced by either Pt or $Pt_{99}Ni_1$. This finding may likely be due to the very high amount of Pt incorporated within these ultrathin NW samples, which is not conducive to these types of reactions.

By contrast, for the Pt_9Ni_1 and Pt_7Ni_3 samples, there was a significant increase in CO_2 formed from CO after the reduction step. The amount of CO_2 generation is perceptible at 90 °C and increased steadily, as the reaction temperature was raised to 140 °C. We also observed that as the samples were cooled down, a decrease in CO_2 performance was noted at the same temperatures. This finding is likely due to the poisoning of the active sites on the Pt, due to the presence of the CO species. Since this reaction does not occur in an acidic electrolyte, Ni sites present on the surface will be stable and can facilitate the reaction through a bifunctional effect.

Based on our XAS analysis, we observed that in samples processed after the "post annealing" treatment, there was an increased degree of alloying between Pt and Ni and a higher probability for Ni to be at the surface of the nanowire. Thus, annealing could yield a proportionately greater quantity of Ni atoms on the external surfaces of these NWs. Ni nanostructures oxidize in air at temperatures ranging from 300 °C to 450 °C depending on the particle size and morphology. It is therefore plausible that the Ni surface sites oxidize and facilitate the oxidation and removal of CO from the Pt sites.

From our XAS results in Figure S2, the annealing process reduces the intensity of the L_3 adsorption peaks for the Pt_9Ni and $Pt_{99}Ni$ to approximately the same intensity as that of Pt foil. This suggests that the annealing process and the higher degree of uniformity of the alloy decrease the beneficial electronic effects observed in the unannealed samples. Since there is no longer any evidence of an electronic effect, these results imply that the enhancement in activity after annealing arises solely from a bifunctional effect of the increased Ni content present at the surface.

Such a structure-induced effect would presumably lead to the observed enhancement in the catalytic oxidation process of CO to CO_2. This type of scenario indicates the importance and necessity of not only a high enough doping quantity of Ni within as-prepared alloys but also the presence of the annealing step itself in ensuring the formation of CO_2. The reason therefore that we observed very little if any CO oxidation activity in all of the "pre-reduction"-processed samples may likely be ascribed to the presence of the highly Pt rich shell as the predominant motif within our wires, as determined by our EXAFS analysis. Specifically, if Pt is preferentially located on the external surface as the predominant majority species, then the distribution of active sites on the wires will be largely unchanged, regardless of the amount of incorporated Ni.

Conclusions

We have successfully synthesized ultrathin nanowires of Pt, $Pt_{99}Ni_1$, Pt_9Ni_1, and Pt_7Ni_3 using a surfactant- mediated method. We collected MOR, FAOR, and EOR data on these samples, and found that the Pt_7Ni_3 system yielded the best performance metrics. Through complementary chronoamperometry runs, we observed that the sample with the highest Ni content delivered the greatest resistance to CO poisoning. CO oxidation experiments demonstrated that the sample with increased Pt loading led to the most improvement in CO_2 production after the samples had been previously exposed to a reducing atmos-

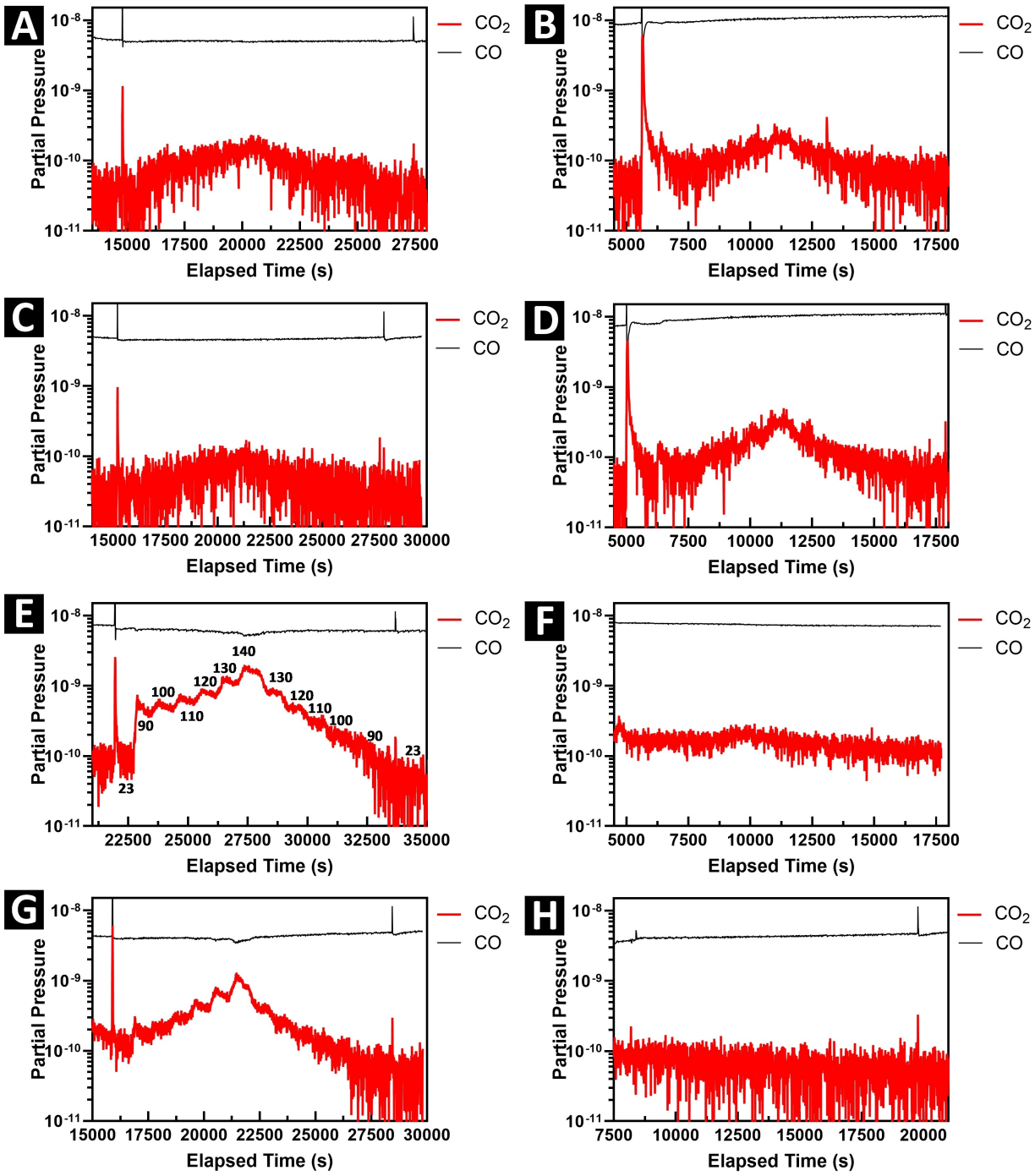

Figure 11. CO oxidation data for (A, B) pure Pt, (C, D) $Pt_{99}Ni_1$, (E, F) Pt_9Ni_1, and (G, H) Pt_7Ni_3. The left-hand column refers to samples prepared after reduction in H_2. The right-hand column corresponds to samples with no reduction performed.

phere. Coupled with an analysis of XAS data, we were able to establish that this scenario is likely caused by the presence of increased alloying of Pt and Ni after an annealing treatment in H_2.

The results of our catalysis measurements highlight two beneficial aspects of PtNi alloys that can be tuned for optimal oxidation performance, depending upon the reaction conditions. In acidic media, surface Ni sites are unstable, and therefore any synergistic effects between surface Pt and Ni sites via a bifunctional effect are not possible. Under these solution conditions, it is most beneficial therefore to utilize as-synthesized PtNi alloys, since the segregation of Ni in the core modulates the electronic properties of the Pt and can lead to improved CO tolerance. By contrast, in the gas phase, surface Ni sites are stable, and therefore Ni can take part in the oxidation mechanism. Under these particular reaction conditions, it is most beneficial to pre-treat the PtNi alloy so as to more evenly distribute the Ni species throughout the structure and increase

the probability of Ni being located at the surface. Although this scenario reduces the benefits of any electronic effects relative to that of the as-prepared nanowires, Ni is more oxophilic than Pt and can oxidize at relatively low temperatures, thereby potentially allowing for the formation of active sites where CO oxidation can occur on the Pt surface. Collectively, our results not only demonstrate an enhancement in catalytic activity but also highlight the importance of examining the spatial distribution of elements throughout a structure in order to more completely understand how composition impacts the observed catalysis.

Experimental Section

Materials. All chemicals were used without further purification. Dihydrogen hexachloroplatinate (IV) hexahydrate (99.9%), boron nitride (99.5%), and anhydrous ethanol denatured (99%) were purchased from Beantown Chemical. Chloroform (ACS grade) was acquired from VWR. Vulcan carbon XC-72 was procured from Fuel Cell Earth. Deionized water was produced on site, whereas ultrapure water was generated using a Milli-pore IQ-7000 system. Hexadecyltrimethylammonium bromide (98%) and ethanol (Uvasol grade) were each obtained through Millipore Sigma. Nickel chloride, perchloric acid (Optima grade), and methanol (Optima grade) were separately purchased from Fisher Scientific. Sodium borohydride (98%) was bought from Alfa Aesar. Formic acid (98+%) was acquired from Acros Organics. The commercial Pt/C TEC10E50E standard consisting of 46.5% platinum was secured from Tanaka Precious Metals.

Pt/PtNi Ultrathin NW Synthesis. Pt and PtNi NWs were fabricated using a modified soft-template synthesis,[19] with which we have significant experience. Specifically, we mixed in 20 mM of an aqueous solution containing Pt and Ni precursors in the presence of 15 mL CTAB in 120 mL DI water within a 500 mL round bottom flask. We subsequently stirred the mixture for 30 mins and then added in 0.6 g of $NaBH_4$ in 15 ml cold water. We allowed it to stir for 20 min, prior to collection by centrifugation and washing of the precipitate with ethanol for 5x.

CO Oxidation Measurements. CO oxidation measurements were carried out in a Claussen cell under an atmosphere of 1% CO and 2% O_2 with 97% He used as the carrier gas. Samples are run before and after an annealing process in a reducing environment, consisting of flowing in 5% H_2 at 300 °C for 2 h. The resulting partial pressure data were collected on a Hiden Analytical QGA, Model No. HAS-301-1551 A mass spectrometer. Measurements were obtained at different temperatures from room temperature to 140 °C, with the temperature systematically increased in intervals of 10 °C.

Electrochemical Measurements

Prior to electrochemical characterization, samples of PtNi NWs were supported onto Vulcan carbon and rendered into catalyst inks by dispersing the dry powders into ethanol, to create an ~1.5 mg/mL solution. A glassy carbon rotating disk electrode (GC-RDE, Pine Instruments, 5 mm) was polished, using an aluminum oxide powder (average particle size of 0.3 μm). Four 5 μL drops of the catalyst ink were then loaded onto the glassy carbon electrode. Each drop was dried under vacuum, before adding in the next. One 5 μL drop of an ethanolic 0.025% Nafion solution was used to seal in the catalyst.

A three-electrode electrochemical cell was assembled with a Pt counter electrode coupled with an $Ag/AgCl_3$ electrode, serving as the reference electrode. Electrochemical measurements of PtNi/C were performed using a 0.1 M perchloric acid (Optima grade) solution electrolyte, generated from high-purity type 1 water with a resistance of 18.2 MΩ cm. Cyclic voltammogram (CV) curves were collected within an Ar-saturated electrolyte solution, at a scan rate of 20 mV/s. The catalytic activity toward the oxidation of small organic molecules (SOMs) was measured via linear sweep voltammograms at a scan rate of 20 mV/s within a solution mixture, containing de-oxygenated 0.1 M perchloric acid and 0.5 M of either methanol, ethanol, or formic acid. Chronoamperometry measurements were obtained with the same solution by stepping the voltage from 0.0 V to 0.7 V vs. RHE and monitoring the current transient for a period of 3600 s. CO stripping measurements were carried out after bubbling in CO for 40 minutes in order to ensure complete coverage of the outer catalyst surface.

Structural and chemical characterization

Transmission Electron Microscopy (TEM). Transmission electron microscopy (TEM) images were collected with the JEOL 1400 transmission electron microscope, operating at an accelerating voltage of 120 kV. The instrument was also equipped with a 2048×2048 Gatan CCD camera. Appropriate nanowire samples were prepared for TEM imaging by sonicating the samples dispersed in ethanol and drop casting aliquots onto Cu grids which were coated with lacey carbon. TEM images were quantitatively analyzed with the use of the ImageJ software to record measurements of average size and standard deviation.

High Resolution Transmission Electron Microscopy (HRTEM/EDS). High angle annular dark field (HAADF) images and HRTEM EDS mapping data were obtained on an FEI Talos F200X instrument, working at 200 KV and equipped with a four-quadrant 0.9-sr energy dispersive X-ray spectrometer (EDS) for both elemental and more broadly speaking, compositional mapping.

X-ray Diffraction (XRD). Collecting X-ray diffraction (XRD) patterns enabled insights into the crystal structure and chemical composition of the NWs. The measurements were carried out on a Rigaku MiniFlex 600 X-ray diffractometer. The instrument was operated at voltage-current conditions of 40 kV and 15 mA, using Cu Kα radiation (λ = 1.5406 Å). The samples were prepared for powder XRD by sonicating the NW powder, which had been dispersed in 5 mL of ethanol. Aliquots of the sample were then drop cast onto a Si zero background diffraction plate for XRD (MTI Corporation, p-type and B-doped silicon, with a 23.6 mm diameter and a 2 mm thickness). Measurements were collected from 2θ values of 10°–90° at a rate of 10°/min, using a scan step of 0.02°/scan. XRD patterns were analyzed using the Match! program.

X-ray absorption spectroscopy (XAS). Relevant XAS measurements were acquired at the National Synchrotron Light Source II (NSLS-II) at the QAS (7-BM) beamline, located at Brookhaven National Laboratory. Data on the Pt L_3 edge (11564 eV) and the Ni K edge (8333 eV) were collected in fluorescence mode using a double crystal Si(111) monochromator. The metal foil reference spectra were obtained simultaneously for each sample and used for energy alignment during data processing. The Demeter software package was used for data processing and analysis.[34]

Thermogravimetric analysis (TGA). The actual loading amounts of NWs deposited onto Vulcan carbon were confirmed by TGA using a TA Instruments Q500. Powders were dried and then loaded into a clean 50 μL Pt pan. These were subsequently heated to 600 °C at a rate of 10°/min and held at this temperature for 10 minutes. This relatively high temperature was chosen to ensure the complete

degradation of any organic components, including the Vulcan carbon supports. Compressed air and anhydrous nitrogen were used as carrier gasses with a flow rate of 40 mL/min and 120 mL/min respectively, throughout the measurements.

Supporting Information

The authors have cited additional references within the Supporting Information.[19,27,28,49,52–75]

Acknowledgements

The synthesis protocols and associated structural characterization reported herein are based on work performed in SSW's laboratory, supported by the U.S. National Science Foundation under Grant No. CHE-1807640. Certain characterization experiments (i.e., TEM, HRTEM, EDS, and SEM) for this manuscript were performed in part at the Center for Functional Nanomaterials, located at Brookhaven National Laboratory, which is supported by the U.S. Department of Energy under Contract No. DE-SC-00112704. Moreover, the collaborative studies were also supported in part by a seed grant from the Stony Brook University Office of the Vice President for Research. AIF acknowledges the support of his work by National Science Foundation under grant CHE 2203858. This research used beamline 7-BM (QAS) of the National Synchrotron Light Source II, a U.S. Department of Energy (DOE) Office of Science User Facility operated for the DOE Office of Science by Brookhaven National Laboratory under Contract No. DE-SC0012704. Beamline operations were supported in part by the Synchrotron Catalysis Consortium (US DOE, Office of Basic Energy Sciences, Grant No. DE-SC0012335). This research used resources of the Center for Functional Nanomaterials, which is a U.S. DOE Office of Science Facility at Brookhaven National Laboratory under Contract No. DE-SC0012704. We thank Drs. Lu Ma, Steven Ehrlich, and Nebojsa Marinkovic for their collective expert help during the synchrotron measurements at QAS beamline.

Conflict of Interests

The authors declare no conflict of interest.

Data Availability Statement

The data that support the findings of this study are available in the supplementary material of this article.

Keywords: alloy formation · electrocatalysis · nanowires · solution-based synthesis · XAS spectroscopy

[1] H. Okamoto, *J. Phase Equilib. Diffus.* **2010**, *31*, 322–322.
[2] A. I. Frenkel, *Chem. Soc. Rev.* **2012**, *41*, 8163–8178.
[3] C. Koenigsmann, M. E. Scofield, H. Liu, S. S. Wong, *J. Phys. Chem. Lett.* **2012**, *3*, 3385–3398.
[4] C. Koenigsmann, S. S. Wong, *Energy Environ. Sci.* **2011**, *4*, 1161–1176.
[5] V. R. Stamenkovic, B. S. Mun, K. J. J. Mayrhofer, P. N. Ross, N. M. Markovic, *J. Am. Chem. Soc.* **2006**, *128*, 8813–8819.
[6] J. Zhang, M. B. Vukmirovic, Y. Xu, M. Mavrikakis, R. R. Adzic, *Angew. Chem. Int. Ed. Engl.* **2005**, *44*, 2132–2135.
[7] S. H. Joo, S. J. Choi, I. Oh, J. Kwak, Z. Liu, O. Terasaki, R. Ryoo, *Nature* **2001**, *412*, 169–172.
[8] C. Koenigsmann, W.-P. Zhou, R. R. Adzic, E. Sutter, S. S. Wong, *Nano Lett.* **2010**, *10*, 2806–2811.
[9] C. Koenigsmann, E. Sutter, R. R. Adzic, S. S. Wong, *J. Phys. Chem. C* **2012**, *116*, 15297–15306.
[10] C. Koenigsmann, E. Sutter, T. A. Chiesa, R. R. Adzic, S. S. Wong, *Nano Lett.* **2012**, *12*, 2013–2020.
[11] N. P. Tarasova, Y. V. Smetannikov, A. A. Zanin, *Russ. Chem. Rev.* **2010**, *79*, 463–477.
[12] X. Teng, M. Feygenson, Q. Wang, J. He, W. Du, A. I. Frenkel, W. Han, M. Aronson, *Nano Lett.* **2009**, *9*, 3177–3184.
[13] H. Zhou, W.-p. Zhou, R. R. Adzic, S. S. Wong, *J. Phys. Chem. C* **2009**, *113*, 5460–5466.
[14] W.-P. Zhou, M. Li, C. Koenigsmann, C. Ma, S. S. Wong, R. R. Adzic, *Electrochim. Acta* **2011**, *56*, 9824–9830.
[15] M. E. Scofield, Y. Zhou, S. Yue, L. Wang, D. Su, X. Tong, M. B. Vukmirovic, R. R. Adzic, S. S. Wong, *ACS Catal.* **2016**, *6*, 3895–3908.
[16] M. E. Scofield, C. Koenigsmann, D. Bobb-Semple, J. Tao, X. Tong, L. Wang, C. S. Lewis, M. B. Vukmirovic, Y. Zhu, R. R. Adzic, S. S. Wong, *Catal. Sci. Technol.* **2016**, *6*, 2435–2450.
[17] H. Liu, R. R. Adzic, S. S. Wong, *ACS Appl. Mater. Interfaces* **2015**, *7*, 26145–26157.
[18] C. Koenigsmann, D. B. Semple, E. Sutter, S. E. Tobierre, S. S. Wong, *ACS Appl. Mater. Interfaces* **2013**, *5*, 5518–5530.
[19] M. E. Scofield, C. Koenigsmann, L. Wang, H. Liu, S. S. Wong, *Energy Environ. Sci.* **2015**, *8*, 350–363.
[20] J. Gu, G. Lan, Y. Jiang, Y. Xu, W. Zhu, C. Jin, Y. Zhang, *Nano Res.* **2014**, *8*, 1480–1496.
[21] J. Yang, G. Ning, L. Yu, Y. Wang, C. Luan, A. Fan, X. Zhang, Y. Liu, Y. Dong, X. Dai, *J. Mater. Chem. A* **2019**, *7*, 17790–17796.
[22] O. Seo, S. A. Oh, J. Y. Lee, S. S. Ha, J. M. Kim, J. W. Choi, J.-W. Kim, H. C. Kang, D. Y. Noh, *J. Alloys Compd.* **2016**, *667*, 141–145.
[23] L. Liu, Y. Wu, F. Chi, Z. Yi, H. Wang, W. Li, Y. Zhang, X. Zhang, *Electrochim. Acta* **2019**, *316*, 125–132.
[24] S. Gao, X. Yang, S. Liang, Y.-H. Wang, H.-Y. Zang, Y.-G. Li, *Inorg. Chem. Commun.* **2019**, *106*, 104–110.
[25] L. Li, H. Liu, C. Qin, Z. Liang, A. Scida, S. Yue, X. Tong, R. R. Adzic, S. S. Wong, *ACS Appl. Nano Mater.* **2018**, *1*, 1104–1115.
[26] H. Liu, C. Koenigsmann, R. R. Adzic, S. S. Wong, *ACS Catal.* **2014**, *4*, 2544–2555.
[27] M. A. van Spronsen, J. W. M. Frenken, I. M. N. Groot, *Chem. Soc. Rev.* **2017**, *46*, 4347–4374.
[28] F. Cai, S. Shan, L. Yang, B. Chen, J. Luo, C.-J. Zhong, *Sci. China Chem.* **2014**, *58*, 14–28.
[29] N. A. Merrill, E. M. McKee, K. C. Merino, L. F. Drummy, S. Lee, B. Reinhart, Y. Ren, A. I. Frenkel, R. R. Naik, N. M. Bedford, M. R. Knecht, *ACS Nano* **2015**, *9*, 11968–11979.
[30] M. R. Knecht, M. G. Weir, A. I. Frenkel, R. M. Crooks, *Chem. Mater.* **2008**, *20*, 1019–1028.
[31] R. M. Anderson, L. Zhang, J. A. Loussaert, A. I. Frenkel, G. Henkelman, R. M. Crooks, *ACS Nano* **2013**, *7*, 9345–9353.
[32] A. I. Frenkel, Q. Wang, S. I. Sanchez, M. W. Small, R. G. Nuzzo, *J. Chem. Phys.* **2013**, *138*, 064202.
[33] S. C. McGuire, A. M. Ebrahim, N. Hurley, L. Zhang, A. I. Frenkel, S. S. Wong, *Chem. Sci.* **2021**, *12*, 7158–7173.
[34] B. Ravel, M. Newville, *J. Synchrotron Radiat.* **2005**, *12*, 537–541.
[35] H. Lei, H. Ryu, A. I. Frenkel, C. Petrovic, *Phys. Rev. B* **2011**, *84*, 214511–214516.
[36] J.-C. Zheng, A. I. Frenkel, L. Wu, J. Hanson, W. Ku, E. S. Božin, S. J. L. Billinge, Y. Zhu, *Phys. Rev. B* **2010**, *81*, 144203.
[37] M. S. Nashner, A. I. Frenkel, D. L. Adler, J. R. Shapley, R. G. Nuzzo, *J. Am. Chem. Soc.* **1998**, *119*, 7760.
[38] Y. Liu, M. Xie, N. Marcella, A. Foucher, E. A. Stach, M. R. Knecht, A. I. Frenkel, *ACS Appl. Nano Mater.* **2022**, *5*, 8775–8782.
[39] R. L. Lawrence, M. O. Olagunju, Y. Liu, K. Mahalingam, J. M. Slocik, R. R. Naik, A. I. Frenkel, M. R. Knecht, *Catal. Sci. Technol.* **2021**, *11*, 2386–2395.

[40] N. Marcella, Y. Liu, J. Timoshenko, E. Guan, M. Luneau, T. Shirman, A. M. Plonka, J. E. S. van der Hoeven, J. Aizenberg, C. M. Friend, A. I. Frenkel, *Phys. Chem. Chem. Phys.* **2020**, *22*, 18902–18910.
[41] S. C. McGuire, A. M. Ebrahim, N. Hurley, L. Zhang, A. I. Frenkel, S. S. Wong, *Chem. Sci.* **2021**, *12*, 7158–7173.
[42] R. Loukrakpam, J. Luo, T. He, Y. Chen, Z. Xu, P. N. Njoki, B. N. Wanjala, B. Fang, D. Mott, J. Yin, J. Klar, B. Powell, C.-J. Zhong, *J. Phys. Chem. C* **2011**, *115*, 1682–1694.
[43] J. M. Cowley, *Phys. Rev.* **1965**, *138*, 1384–1389.
[44] A. I. Frenkel, V. Sh. Machavariani, A. Rubshtein, Y. Rosenberg, A. Voronel, E. A. Stern, *Phys. Rev. B* **2000**, *62*, 9364–9371.
[45] K.-W. Park, J.-H. Choi, B.-K. Kwon, S.-A. Lee, Y.-E. Sung, H.-Y. Ha, S.-A. Hong, H. Kim, A. Wieckowski, *J. Phys. Chem. B* **2002**, *106*, 1869–1877.
[46] S. Rudi, L. Gan, C. Cui, M. Gliech, P. Strasser, *J. Electrochem. Soc.* **2015**, *162*, F403-F409.
[47] J. Zhang, Y. Mo, M. B. Vukmirovic, R. Klie, K. Sasaki, R. R. Adzic, *J. Phys. Chem. B* **2004**, *108*, 10955–10964.
[48] R. R. Adzic, J. Zhang, K. Sasaki, M. B. Vukmirovic, M. Shao, J. X. Wang, A. U. Nilekar, M. Mavrikakis, J. A. Valerio, F. Uribe, *Top. Catal.* **2007**, *46*, 249–262.
[49] N. Smina, A. Rosen, L. Sztaberek, W. Beatrez, K. Kingsbury, R. Troia, Y. Wang, J. Zhao, J. Schrier, C. Koenigsmann, *ACS Appl. Mater. Interfaces* **2021**, *13*, 59892–59903.
[50] H. Q. Pham, T. T. Huynh, *Dalton Trans.* **2022**, *51*, 11427–11436.
[51] H. Quoc Pham, T. Thien Huynh, S. Truong Nguyen, N. Nguyen Dang, L. Giang Bach, V. Thi Thanh Ho, *Fuel* **2020**, *276*, 118078.
[52] W. Zhang, Y. Yang, B. Huang, F. Lv, K. Wang, N. Li, M. Luo, Y. Chao, Y. Li, Y. Sun, Z. Xu, Y. Qin, W. Yang, J. Zhou, Y. Du, D. Su, S. Guo, *Adv. Mater.* **2019**, *31*, 1805833–1805842.
[53] Y. Wang, J. Zang, L. Dong, H. Pan, Y. Yuan, Y. Wang, *Electrochim. Acta* **2013**, *113*, 583–590.
[54] Y. Shu, L. E. Murillo, J. P. Bosco, W. Huang, A. I. Frenkel, J. G. Chen, *Appl. Catal. A* **2008**, *339*, 169–179.
[55] T. Xia, K. Zhao, Y. Zhu, X. Bai, H. Gao, Z. Wang, Y. Gong, M. Feng, S. Li, Q. Zheng, S. Wang, R. Wang, H. Guo, *Adv. Mater.* **2023**, *35*, 2206508.
[56] X. Zhao, C. Xi, R. Zhang, L. Song, C. Wang, J. S. Spendelow, A. I. Frenkel, J. Yang, H. L. Xin, K. Sasaki, *ACS Catal.* **2020**, *10*, 10637–10645.
[57] Q. Wang, R. Zhu, P. Deng, J. Li, W. Huang, Q. Chen, Y.-Q. Su, C. Jia, Z. Liu, Z. Kang, Y. Shen, X. Tian, *Sci. China Mater.* **2022**, *66*, 679–685.
[58] W. Zhang, Y. Yang, B. Huang, F. Lv, K. Wang, N. Li, M. Luo, Y. Chao, Y. Li, Y. Sun, Z. Xu, Y. Qin, W. Yang, J. Zhou, Y. Du, D. Su, S. Guo, *Adv. Mater.* **2019**, *31*, 1805833–1805842.
[59] T. Tamaki, Y. Yamada, H. Kuroki, T. Yamaguchi, *J. Electrochem. Soc.* **2017**, *164*, 858–860.
[60] S. Wang, G. Yang, S. Yang, *J. Phys. Chem. C* **2015**, *119*, 27938–27945.
[61] Q. Jiang, L. Jiang, H. Hou, J. Qi, S. Wang, G. Sun, *J. Phys. Chem. C* **2010**, *114*, 19714–19722.
[62] M. Li, K. Duanmu, C. Wan, T. Cheng, L. Zhang, S. Dai, W. Chen, Z. Zhao, P. Li, H. Fei, Y. Zhu, R. Yu, J. Luo, K. Zang, Z. Lin, M. Ding, J. Huang, H. Sun, J. Guo, X. Pan, W. A. Goddard, P. Sautet, Y. Huang, X. Duan, *Nat. Catal.* **2019**, *2*, 495–503.
[63] M. Li, Y. Cai, J. Zhang, H. Sun, Z. Li, Y. Liu, X. Zhang, X. Dai, F. Gao, W. Song, *Nano Res.* **2021**, *15*, 3230–3238.
[64] L. Zhang, Q. Chang, H. Chen, M. Shao, *Nano Energy* **2016**, *29*, 198–219.
[65] L. Chen, J. Zhu, C. Xuan, W. Xiao, K. Xia, W. Xia, C. Lai, H. L. Xin, D. Wang, *J. Mater. Chem. A* **2018**, *6*, 5848–5855.
[66] J. Chang, L. Song, Y. Xu, Y. Ma, C. Liang, W. Jiang, Y. Zhang, *Nano Res.* **2019**, *13*, 67–71.
[67] H. Zhang, X. Wang, A. I. Frenkel, P. Liu, *J. Chem. Phys.* **2021**, *154*, 014702.
[68] G. Samjeské, M. Osawa, *Angew. Chem.* **2005**, *117*, 5840–5844.
[69] G. Ren, Y. Liu, W. Wang, M. Wang, Z. Zhang, Y. Liang, S. Wu, J. Shen, *ACS Appl. Nano Mater.* **2018**, *1*, 3226–3235.
[70] F. Wu, K. Eid, A. M. Abdullah, W. Niu, C. Wang, Y. Lan, A. A. Elzatahry, G. Xu, *ACS Appl. Mater. Interfaces* **2020**, *12*, 31309–31318.
[71] F. Liu, J. Y. Lee, W. Zhou, *J. Phys. Chem. B* **2004**, *108*, 17959–17963.
[72] F. Gao, Y. Zhang, P. Song, J. Wang, B. Yan, Q. Sun, L. Li, X. Zhu, Y. Du, *Nanoscale* **2019**, *11*, 4831–4836.
[73] D. Liu, Y. Li, M. Kottwitz, B. Yan, S. Yao, A. Gamalski, D. Grolimund, O. V. Safonova, M. Nachtegaal, J. G. Chen, E. A. Stach, R. G. Nuzzo, A. I. Frenkel, *ACS Catal.* **2018**, *8*, 4120–4131.
[74] A. B. A. A. Nassr, I. Sinev, W. Grünert, M. Bron, *Appl. Catal. B.* **2013**, *142–143*, 849–860.
[75] A. B. A. A. Nassr, I. Sinev, M.-M. Pohl, W. Grünert, M. Bron, *ACS Catal.* **2014**, *4*, 2449–2462.

Manuscript received: September 24, 2023
Revised manuscript received: October 29, 2023
Accepted manuscript online: November 1, 2023
Version of record online: December 6, 2023